Tracing the physical and chemical evolution of low-mass protostars

Jørgensen, J.K.

Chapter 9

Passive heating vs. shocks in protostellar environments

CH_3OH and H_2CO in the envelopes around low-mass protostars

Abstract

This chapter presents the third in a series of single-dish studies of molecular abundances in the envelopes around a large sample of 18 low-mass pre- and protostellar objects, concluding the molecular line survey also described in Chapters 2 and 3. It focuses on typical grain mantle products and organic molecules, including H_2CO, CH_3OH and CH_3CN. With a few exceptions, all H_2CO lines can be fit by constant abundances throughout the envelopes if ortho- and para lines are considered independently. The current observational dataset does not require a large jump in the inner warm regions, but also this cannot be ruled out. Through comparison of the H_2CO abundances of the entire sample, the H_2CO ortho-para ratio is constrained to be 1.6 ± 0.3 consistent with thermalization on grains at temperatures of 10–15 K. The H_2CO abundances can be related to the empirical chemical network established on the basis of our previously reported survey of other species and is found to be closely correlated with that of the nitrogen-bearing molecules. These correlations reflect the freeze-out of molecules at low temperatures and high densities, with the constant, radius independent, H_2CO abundance being a measure of the amount of material in the region where this occurs. An improved fit to the data is obtained with a drop abundance structure, where the freeze-out zone is constrained from CO observations. The CH_3OH lines are found to be significantly broader than the H_2CO lines, indicating that they probe kinematically distinct regions. CH_3OH is moreover only detected toward a handful of sources and CH_3CN toward only one, NGC 1333-IRAS2. For NGC 1333-IRAS2, jumps in abundances of CH_3OH and CH_3CN at 90 K of two-three orders of magnitude are found. In contrast, the NGC 1333-IRAS4A and IRAS4B CH_3OH data are fitted with a constant abundance and a jump at a lower temperature of 30 K, respectively. This is consistent with a scenario where the CH_3OH probes the action of compact outflows on the envelopes, which is further supported by comparison to high frequency, high excitation CS $J = 10$–9 and HDO observations. The extent to which the outflow dominates the abundance jumps compared with the passively heated inner envelope depends on the filling factors of the two components in the observing beam.

Jørgensen, Schöier & van Dishoeck, 2004, A&A, in prep.

9.1 Introduction

The chemistry of organic molecules in the envelopes around low-mass protostars is likely to reflect directly in the molecular composition of their circumstellar disks and eventual protoplanetary systems. A number of competing mechanisms are important in regulating the chemistry in these early deeply embedded stages: the heating of protostellar cores due to central, newly formed stars results in evaporation of ices in the innermost regions whereas shocks related to the ubiquitous outflows may liberate ice mantles and trigger similar effects but on larger scales. These mechanisms have been suggested to be the cause of enhancements of, e.g., H_2O, H_2CO and CH_3OH on small scales in the envelopes (e.g., Ceccarelli et al. 1998, 2000a; Schöier et al. 2002, 2004a). This chapter presents an analysis of, in particular, H_2CO and CH_3OH abundances in the sample of 18 protostars studied in a wide range of other molecules by Jørgensen et al. (2002, 2004d) (Chapters 2 and 3). Those chapters discussed observations of molecular species predominantly probing the outer cold envelopes around these objects. It was found that freeze-out at low temperatures and high densities dominates the chemistry and that, in particular, the freeze-out of CO is reflected in the abundances of a number of related species at large distances from the central protostar. This paper complements the study of H_2CO and CH_3OH in a subset of objects by Maret et al. (2004a,b). Both species are typical grain-mantle products observed in interstellar ices. To fully appreciate their chemistry it is also important to compare their abundances with the more general chemical network, especially since the high resolution observations of Schöier et al. (2004a) (Chapter 7) indicate that the H_2CO abundance structures may be related to the "drop abundance" structures inferred from CO observations (Jørgensen et al. 2004c) (Chapter 4). Furthermore, CH_3CN and high excitation CS and HDO observations are presented, illustrating the relative importance of shocks and passive heating from the central protostar.

The class 0 protostar, IRAS 16293-2422, has long been the template for astrochemistry studies of deeply embedded low-mass protostars due to its rich spectrum (Blake et al. 1994; van Dishoeck et al. 1995). IRAS 16293-2422 has a central warm and dense gas core where ices evaporate. Recently, Cazaux et al. (2003) have shown the existence of a large number of complex organic species in IRAS 16293-2422, further underscoring the rich chemistry of this particular source. It remains an interesting question whether this simply reflect "first generation" evaporation of organic molecules at high temperatures or whether the timescales are indeed long enough that a "second generation" hot core chemistry can evolve in the innermost regions of these envelopes (see, e.g., discussion in Schöier et al. 2002).

To put the IRAS 16293-2422 results in context, it is important to expand the sample of well-studied protostars. Jørgensen et al. (2004d) presented a survey of molecular species probing the cold outer component of protostellar objects with different envelope masses, i.e., both "class 0" and "class I" objects. Although large variations in abundances occur within the sample, it was found

that IRAS 16293-2422 is in no way unique. The same objects were observed in transitions of H_2CO and CH_3OH at the JCMT. Maret et al. (2004a) presented the H_2CO observations, together with observations from the IRAM 30 m telescope, for a subset of exclusively class 0 objects. They reported the existence (or possibility) of H_2CO abundance jumps, in some cases up to four orders of magnitude. However, Schöier et al. (2004a) show through high angular resolution data of IRAS 16293-2422 and L1448-C, that the exact abundance structure of the outer envelopes may severely affect the interpretation of the innermost ($T > 90$ K) envelope. For these low luminosity sources the warm inner regions have diameters < 100 AU ($< 0.5''$), i.e., are significantly diluted for typical single-dish observations.

Buckle & Fuller (2002) studied the low excitation ($3_K - 2_K$) lines of CH_3OH toward a large sample of class 0 and I objects. They found that a large fraction of the sources, predominantly the class 0 objects, show lines with two velocity components with CH_3OH being enhanced by up to two orders of magnitude. Buckle & Fuller suggest that the broad component is due to outflow generated shocks heating the envelope material and thus liberating the grain mantles. Similar effects are also observed in several well-studied "isolated" outflows (Bachiller et al. 1995; Bachiller & Pérez Gutiérrez 1997; Jørgensen et al. 2004a, Chapter 8). Their discussion illustrates that for CH_3OH, a big issue may be whether the abundances derived from single-dish observations toward protostellar cores are related to passive heating or the action of outflows.

This chapter expands the work of Maret et al. (2004a,b) through modeling of H_2CO, CH_3OH and CH_3CN emission for the entire sample of pre- and protostellar cores studied by Jørgensen et al. (2002, 2004d), adopting the same physical models and approach as in these papers. In addition, we present high excitation CS $J = 10 - 9$ and HDO observations which uniquely probe the dense and warm gas in the envelope. Sect. 9.2 presents the observations forming the basis of this study. Sect. 9.3 describes the model approach, highlighting the similarities and differences with the work of Maret et al. (2004a). Sect. 9.4 discusses the results, focusing on the distinction between passively heated and shock processed material. Based on this study, it is discussed which objects are good candidates for further studies of low-mass protostellar "hot cores".

9.2 Observations

9.2.1 General issues

The sample of 18 pre- and protostars presented by Jørgensen et al. (2002) was observed in a wide range of lines at the James Clerk Maxwell Telescope from 2001 through 2003. The observations of other species besides H_2CO, CH_3OH and CH_3CN are discussed by Jørgensen et al. (2004d). Maret et al. (2004a,b) reported H_2CO and CH_3OH observations, respectively, toward the sources with the most massive envelopes - and hence strongest lines - in the sample, which are also included in this paper. The following sections discuss the observations of each of these species in detail. All lines were observed and reduced in a

standard way: pointing was checked regularly at the telescope and typically found to be accurate to within a few arcseconds. Calibration was checked by observations of line standards and found to be accurate to within 20%. The A3 and B3 receivers at 1.3 and 0.8 mm were used: the telescope beam sizes are typically 21″ and 14″ at these frequencies. The velocity resolution ranged from 0.13 to 0.55 km s^{-1} for the different line settings. Low order polynomials were subtracted and the spectra were brought onto the $T_{\rm MB}$ scale by division by the main beam efficiencies, $\eta_{\rm MB}$ at the relevant frequencies given on the JCMT web page[1].

In addition to these observations, the high frequency RxW receiver was used to observe CS $J = 10 - 9$ at 489.751 GHz for four sources (L1448-C, NGC 1333-IRAS2, -IRAS4A and -IRAS4B) over two nights in November 2002. Special care was taken with the calibration: comparison with nearby spectral standards was found to vary by $< 20\%$ over these two nights, during which the sky opacity was $\lesssim 0.05$ at 225 GHz and the elevation of the sources higher than $\approx 50^\circ$. Still, high system temperatures of up to $\sim$ 5000 K were found and this, together with the pointing uncertainties of a few arcseconds of the JCMT (compared to a beam size of 10″), may cause the absolute calibration to be somewhat uncertain for these observations.

Most of the observed CH_3OH lines are remarkably symmetric and for these lines, a single Gaussian could be fitted. The only exceptions are a few of the lowest excitation lines, which are integrated over ± 2 km s^{-1} from the systemic velocity. The line intensities for all species are given in Tables 9.1–9.4. For the non-detections, 3σ upper limits are reported with $\sigma = 1.2\sqrt{\delta v\, \Delta_0 v}\, T_{\rm RMS}$ where δv is the velocity resolution, $\Delta_0 v$ the expected line width to zero intensity (assumed to be 4 km s^{-1}), $T_{\rm RMS}$ the RMS noise level for the given resolution and the factor 1.2 introducing the 20% calibration uncertainty.

9.2.2 H_2CO

In addition to the observations presented by Maret et al. (2004a), H_2CO emission from the ortho $5_{15} - 4_{14}$ line at 351.768 GHz and the para $5_{05} - 4_{04}$ line at 362.736 GHz was observed for all sources. Furthermore JCMT archival data exist for the para $3_{03} - 2_{02}$ and $3_{22} - 2_{21}$ lines at 218.222 and 218.475 GHz for most sources and these observations were included. Table 9.1 lists the line intensities for all sources. The typical line widths of the H_2CO lines were 1.5–2 km s^{-1} (FWHM). For the prestellar cores, L1544 and L1689B, intensities of lines at 1 mm from IRAM 30 m observations by Bacmann et al. (2003) were included in the modeling.

9.2.3 CH_3OH

Tables 9.2–9.3 summarize the observed line intensities for CH_3OH. Only the NGC 1333 sources have detections for a large number of CH_3OH lines. Besides

[1] `http://www.jach.hawaii.edu/JCMT`

Table 9.1. *Integrated H_2CO line intensities ($\int T_{\rm MB}\,{\rm d}v$).*

	p-H_2CO			o-H_2CO
	$3_{03}-2_{02}$[a]	$3_{22}-2_{21}$[a]	$5_{05}-4_{04}$	$5_{15}-4_{14}$
L1448-I2	...	...	<0.9	1.2
L1448-C[b]	3.4	0.4	1.3	1.0
N1333-I2[b]	4.9	1.0	1.8	1.6
N1333-I4A[b]	9.3	2.2	2.9	5.5
N1333-I4B[b]	9.6	4.7	5.9	7.5
L1527[b]	3.0	0.2	0.4	1.0
VLA1623[b]	5.0	...	1.2	0.9
L483	2.3	<0.2	1.2	1.3
L723	1.1[c]	<0.1[c]	1.1	2.0
L1157[b]	1.1	<0.3	0.5	1.2
CB244	0.9	<0.4	0.6	1.4
L1489	<0.3	<0.3	<0.4	0.7
TMR1	0.6	<0.1	<0.3	0.4
L1544	0.3[d]	...	<0.5	<0.4
L1689B	1.7[d]	1.0[d]	<0.3	<0.4

[a] $3_{03}-2_{02}$ and $3_{22}-2_{21}$ line intensities from Maret et al. (2004a) are from IRAM 30 m observations. [b] Observations previously reported by Maret et al. (2004a). For some of these sources additional o-H_2CO $2_{12}-1_{11}$ and $4_{14}-3_{13}$, p-H_2CO $5_{24}-4_{23}$ and o-$H_2^{13}CO$ observations and limits were reported by Maret et al. (2004a). [c] From SEST (HPBW=24″) observations. [d] IRAM 30 m observations from Bacmann et al. (2003): for these two pre-stellar cores o-H_2CO $2_{12}-1_{11}$ observations were also reported by Bacmann et al. and included in the modeling.

these, only L723, L1448-C and VLA 1623 show detections in the 7_K-6_K band and only of 1–2 lines each. In addition to the observations of the 7_K-6_K lines also presented by Maret et al. (2004b), the 5_K-4_K band at 241 GHz was also observed for the NGC 1333 sources.

As for H_2CO, the CH_3OH lines can be divided into two forms, A- and E-type, depending on the orientation of the methyl CH_3-group with respect to the OH group. Table 9.2 lists the line intensities for the NGC 1333 sources and Table 9.3 those for the remaining sources. Some systematics, which may give clues to the origin of the CH_3OH emission, can be directly inferred from these results. For example, NGC 1333-IRAS2 shows the highest excitation lines both for the A and E-type for the 5_K-4_K and 7_K-6_K transitions compared to NGC 1333-IRAS4A and -IRAS4B. Still, the lowest excitation lines toward NGC 1333-IRAS2 are weaker than those toward the NGC 1333-IRAS4 sources: barring pure excitation/opacity effects, this could be interpreted as a warmer interior, possibly with higher abundances in NGC 1333-IRAS2. In particular,

Table 9.2. *CH_3OH line intensities ($\int T_{\rm MB}\,{\rm d}v$) for sources in NGC 1333.*

Line	Frequency	IRAS2	IRAS4A	IRAS4B
$5_K - 4_K$ band; E-type				
+0E	241.7002	0.41	2.9	2.1
$-$1E	.7672	0.86	7.8	4.6
$-$4E	.8132	0.17	$<$0.06	$<$0.06
+4E	.8296	0.16	$<$0.06	$<$0.06
+3E	.8430	0.30	0.48	0.55 †
$-$3E	.8523	0.17	$<$0.06	$<$0.06
+1E	.8790	0.33	1.3	1.3
$\pm$2E	.9044	0.45	2.7	2.3
$5_K - 4_K$ band; A-type				
+0A	241.7914	1.1	8.9	5.3
$\pm$4A	.8065	0.18	$<$0.06	< 0.06
$\pm$3A	.8329	0.33	0.64	0.53
$-$2A	.8430	0.30	0.48	0.55 †
+2A	.8877	0.23	0.49	0.50
$7_K - 6_K$ band; E-type				
$-$1E	338.3446	1.5	6.2	5.9
$-$4E	.5040	0.34	$<$0.06	$<$0.06
+4E	.5302	0.40	$<$0.06	$<$0.06
$-$3E	.5599	0.34	$<$0.06	$<$0.06
+3E	.5831	0.40	0.17	0.36
+1E	.6150	0.71	1.4	1.7
$7_K - 6_K$ band; A-type				
+0A	338.4086	1.8	7.4	6.8
$\pm$4A/-2A	.5127	0.41	0.49	0.89
$\pm$3A	.5419	0.68	0.75	1.4
+2A	.6399	0.42	0.34	0.58

"†"The $5-4$ +3E and $-$2A lines are blended at 241.8430 GHz and have therefore (although observed) been excluded from the modeling. The quoted intensity refers to the total intensity of both lines.

since the sources otherwise have relatively similar physical structures these differences suggest that one or more sources will show chemical gradients. Furthermore the CH_3OH lines are significantly broader with line widths of 4–5 km s^{-1} (FWHM) compared to 1.5–2 km s^{-1} found for H_2CO and the other species in Jørgensen et al. (2002, 2004d).

Table 9.3. *CH_3OH line intensities and limits for sources not in NGC 1333.*

	7–6	
	-1E	0A+
L1448-I2	< 0.09	
L1448-C	0.254	0.415
L1527	< 0.12	
VLA1623	0.063	0.060
L483	< 0.18	
L723	< 0.06	0.373
L1157	< 0.18	
CB244	< 0.12	
L1489	< 0.09	
TMR1	< 0.09	

Table 9.4. *CH_3CN and CH_3OCH_3 line intensities ($\int T_{\rm MB}\,{\rm d}v$ [K km s^{-1}]) and 3σ upper limits for the sources in NGC 1333.*

Line	Frequency	IRAS2	IRAS4A	IRAS4B
CH_3CN				
14_3–13_3	257.4828	0.20	<0.09	<0.1
14_2–13_2	257.5076	0.10	–	–
14_1–13_1	257.5224	0.17	–	–
14_0–13_0	257.5274	0.15	–	–
CH_3OCH_3				
$13_{1,13}$–$12_{0,12}$	241.9468	<0.08	<0.1	<0.1

9.2.4 CH_3CN and other species

CH_3CN $14_K - 13_K$ was observed at 257.5 GHz for the NGC 1333 sources with 2 hours integration time per source, reaching RMS levels of 0.02 K ($T_{\rm MB}$) in 0.36 km s^{-1} channels. Even at these levels 3σ detections were only found for NGC 1333-IRAS2, as shown in Fig. 9.1. Considering that this source typically show weaker lines for other molecules than the two NGC 1333-IRAS4 sources (see, e.g., Jørgensen et al. 2004d), this suggests that CH_3CN may probe a different chemical regime (together with the CH_3OH lines) than the bulk, cold envelope in this source. The HDO $2_{11} - 2_{12}$ transition at 241.5616 GHz was covered in the CH_3OH $5_K - 4_K$ setting and also only detected toward NGC 1333-IRAS2. CH_3OCH_3 $13_{1,13} - 12_{0,12}$ at 241.95 GHz in the same setting was in contrast not detected toward any of the sources down to the noise limit.

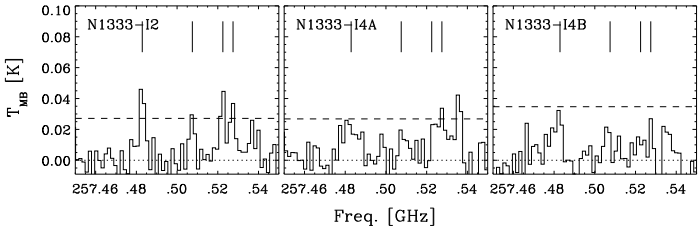

Figure 9.1. *CH_3CN $14_K - 13_K$ line observations at 257.5 GHz of the NGC 1333 sources. The vertical lines indicate the expected locations of the $K = 0, 1, 2, 3$ lines. The dashed line indicates the 3σ detection limit.*

9.3 Modeling

To model the chemical abundances the approach described in Jørgensen et al. (2002, 2004d) and Schöier et al. (2002), and utilized for the entire sample of sources and molecules, was adopted: each species was modeled with the envelope physical structure from Jørgensen et al. (2002) derived from dust radiative transfer modeling of their submillimeter (SCUBA) continuum emission and SEDs. The line radiative transfer was then performed using the code of Schöier et al. (2002) constraining the average molecular abundances. This code was benchmarked to high accuracy against a large number of other line radiative transfer codes for a number of test problems by van Zadelhoff et al. (2002) and found to agree within the Monte Carlo noise.

For H_2CO the collisional rate coefficients used in Schöier et al. (2002) were adopted. As described by Maret et al. (2004a), ortho $H_2^{13}CO$ lines are detected for the three sources in NGC 1333. The corresponding abundances were likewise calculated and taken into account in subsequent discussions. For CH_3OH, new collisional rate coefficients by Pottage et al. (2004) were used. For CH_3CN and CH_3OCH_3, LTE excitation was assumed. The molecular data files are summarized by Schöier et al. (2004b) and publically available[2]. Each of the ortho- and para H_2CO and the A- and E-type CH_3OH were treated as separate molecules, which is possible since radiative transitions between the different species are ruled out. In the first iteration, the abundances are kept constant throughout the envelope and the results from the best fits are given in Tables 9.5-9.9 below.

9.3.1 H_2CO

For most sources the H_2CO line intensities are well-fit with constant abundance models for each of the p-H_2CO and o-H_2CO species. For a few sources, one of these two has a $\chi^2_{\rm red}$ higher than 3 (o-H_2CO: NGC 1333-IRAS4B, L1527, L1157 and L1689B; p-H_2CO: NGC 1333-IRAS4A, L483 and CB244). This is in contrast

[2] `http://www.strw.leidenuniv.nl/~moldata`

Table 9.5. *Inferred abundances for p-H_2CO, reduced χ^2 and number of lines were applicable.*

Source	Abundance	$\chi^2_{\rm red}$	$n_{\rm lines}$
L1448-I2	$<1.8\times10^{-10}$	...	(1)
L1448-C	6.8×10^{-10}	1.0	4
N1333-I2	3.9×10^{-10}	1.3	4
N1333-I4A	2.3×10^{-10}	3.1	4
N1333-I4B	4.1×10^{-9}	0.96	4
L1527	8.4×10^{-10}	0.44	3
VLA1623	1.3×10^{-9}	0.061	2
L483	3.3×10^{-10}	6.7	2
L723	9.6×10^{-10}	2.6	2
L1157	3.6×10^{-11}	2.1	2
CB244	6.9×10^{-10}	10.9	2
L1489	$<1.4\times10^{-9}$	...	(1)
TMR1	3.4×10^{-9}	...	1+(1)
L1544[a]	3.0×10^{-11}	...	1
L1689B[a]	1.2×10^{-10}	0.6	2

[a]Quoted value based on line intensities reported by Bacmann et al. (2003). The upper limits from high excitation lines observed at the JCMT are larger by two orders of magnitude.

to Maret et al. (2004a) who inferred large abundance jumps for the studied sources. As shown below this is due to a number of differences in the assumptions between the work of Maret et al. (2004a) and this study, in particular the ortho-para ratio. Below we discuss some of these differences.

Velocity structure

Maret et al. (2004a) assume a non-turbulent but infalling envelope, whereas our work assumes a constant turbulent broadening throughout the envelope reproducing the observed line widths. The derived abundances do not depend on the velocity field as long as integrated intensities of optically thin lines are considered (Jørgensen et al. 2004d), but this may not be an adequate description of emission originating from the innermost dense regions in the case of large abundance jumps. In the context of an inside-out collapsing envelope, the outer envelope will naturally be characterized by the turbulent broadening. In class 0 objects typical inferred ages are $\sim 10^4$ years, which for typical values of the sound speed of 0.3–0.5 km s^{-1} translate to infall radii of 500–1000 AU. Such sizes are unresolved by single-dish observations and even by medium-high resolution interferometer data. This implies that the infall radius encompasses the hot inner region, but that most of the mass in the envelope material is not

Table 9.6. *Inferred abundances for o-H_2CO and o-$H_2^{13}CO$, reduced χ^2 and number of lines where applicable.*

Source	Abundance	$\chi^2_{\rm red}$	$n_{\rm lines}$
	o-H_2CO		
L1448-I2	3.0×10^{-10}	...	1
L1448-C	8.9×10^{-10}	1.2	3
N1333-I2	4.3×10^{-10}	0.63	3
N1333-I4A	3.4×10^{-10}	0.59	3
N1333-I4B	8.7×10^{-10}	6.2	3
L1527	8.4×10^{-10}	7.7	3
VLA1623	7.7×10^{-10}	0.34	3
L483	6.3×10^{-10}	...	1
L723	3.1×10^{-9}	...	1
L1157	9.2×10^{-11}	3.9	3
CB244	5.3×10^{-9}	...	1
L1489	2.7×10^{-9}	...	1
TMR1	5.0×10^{-9}	...	1
L1544[a]	4.0×10^{-11}	...	1
L1689B[a]	2.0×10^{-10}	8.4	2+(1)
	o-$H_2^{13}CO$		
N1333-I2	3.0×10^{-11}	3.3	2
N1333-I4A	5.2×10^{-12}	2.5	3
N1333-I4B	8.0×10^{-11}	...	1

[a]Upper limits from JCMT lines only are 6×10^{-10}; see footnote a, Table 9.5.

infalling.

From line radiative transfer it is possible to make exact predictions for the line profiles, which can be compared to the observed spectra to constrain the velocity field. Fig. 9.2 compares the observed $5_{05} - 4_{04}$ and $5_{15} - 4_{14}$ spectra toward L1448-C with the modeled line profiles adopting the non-infalling but turbulent envelope model (with constant H_2CO abundance) from this paper and the non-turbulent, infalling model (with abundance jump) from Maret et al. (2004a). Considering only the higher excitation H_2CO $J = 5 - 4$ lines should limit confusion from the surrounding material. It is seen that the "turbulent" envelope model clearly provides the closest match to the observed line profile, whereas the non-turbulent, infalling model provides too much broadening. It is interesting to note that the same turbulent broadening which is used to fit low-excitation CO isotopic lines from the cold, outer envelope (Jørgensen et al. 2002) works well in also explaining the observed H_2CO line widths. In the context of, e.g., an inside-out collapsing envelope as in Shu (1977) this suggests that the infalling region of the envelope is small and that even the relatively

Table 9.7. *Inferred abundances for A-type CH_3OH, reduced χ^2 and number of lines where applicable.*

Source	Abundance	$\chi^2_{\rm red}$	$n_{\rm lines}$
L1448-I2	$<1.1\times10^{-10}$	...	(1)
L1448-C	1.3×10^{-9a}	...	1
N1333-I2	1.4×10^{-9a}	20.4	8
N1333-I4A	2.9×10^{-9a}	4.5	7
N1333-I4B	3.5×10^{-8a}	11.4	7
L1527	$<5.5\times10^{-10}$	...	(1)
VLA1623	2.5×10^{-10}	...	1
L483	$<2.2\times10^{-10}$	...	(1)
L723	1.8×10^{-9}	...	1
L1157	$<2.7\times10^{-10a}$	...	(1)
CB244	$<1.0\times10^{-9}$	...	(1)
L1489	$<9.9\times10^{-10}$	...	(1)
TMR1	$<2.2\times10^{-9}$	...	(1)

[a]See also Maret et al. (2004b).

high excitation H_2CO lines studied in this paper are still predominantly sensitive to the outer envelope. It is worth re-emphasizing that both turbulent and non-turbulent/infalling models give a good constant abundance fit when the ortho and para lines are treated independently and that abundance jumps are in general not required for the studied sources, other than in the context of a "drop model" (see Sect. 9.3.1).

H_2CO ortho-para ratio

A second difference with Maret et al. (2004a) is the assumption of a fixed ortho/para ratio. Since para and ortho H_2CO can be considered to be separate molecules, their abundances can be determined independently. Fig. 9.3 compares the abundances for the two species. A very close correlation exists (Pearson correlation coefficient of 0.9; see also Sect. 9.3.1), which can be fitted by an ortho-para ratio of 1.6±0.3. The very tight correlation indicates that both species probe the same region of the envelope and that their abundance ratios are established under similar conditions in all sources.

Maret et al. (2004a) assumed an ortho-para ratio of 3 to combine o-H_2CO and p-H_2CO line observations to constrain the abundance structure. Whereas this gives in principle fewer free parameters in the modeling, one should be careful when interpreting the results. This is clearly illustrated in Fig. 9.4 where constraints on the total H_2CO abundance from ortho and para lines for L1448-C are shown. It can be seen that the overlapping confidence levels depend critically on the adopted ortho-para ratio, with a high ortho-para ratio driving

Table 9.8. *Inferred abundances for E-type CH_3OH, reduced χ^2 and number of lines where applicable.*

Source	Abundance	$\chi^2_{\rm red}$	$n_{\rm lines}$
L1448-I2	$<1.4\times10^{-10}$	...	(1)
L1448-C	1.0×10^{-9a}	...	1
N1333-I2	1.3×10^{-9a}	18.4	13
N1333-I4A	2.5×10^{-9a}	3.1	7
N1333-I4B	9.1×10^{-9a}	9.6	7
L1527	$<6.8\times10^{-10}$	...	(1)
VLA1623	3.4×10^{-10}	...	1
L483	$<2.7\times10^{-10}$	...	(1)
L723	$<3.6\times10^{-10}$	...	(1)
L1157	$<3.4\times10^{-10a}$	...	(1)
CB244	$<1.3\times10^{-9}$	...	(1)
L1489	$<1.2\times10^{-9}$	...	(1)
TMR1	$<2.8\times10^{-9}$	...	(1)

[a]See also Maret et al. (2004b).

Table 9.9. *Inferred abundances for CH_3CN and CH_3OCH_3 with reduced χ^2 and number of lines where appropriate.*

Source	Abundance	$\chi^2_{\rm red}$	$n_{\rm lines}$
	CH_3CN		
N1333-I2	8.3×10^{-11}	8.5	4
	7×10^{-9a}	1.4	4
N1333-I4A	$<1.8\times10^{-11}$	...	(4)
	$<6\times10^{-10b}$	–	–
N1333-I4B	$<6.4\times10^{-11}$	...	(4)
	$<2\times10^{-7b}$	–	–
	$<3\times10^{-10c}$	–	–
	CH_3OCH_3		
N1333-I2	$<3\times10^{-9}$	...	(1)
N1333-I4A	$<2\times10^{-9}$	...	(1)
N1333-I4B	$<5\times10^{-9}$	...	(1)

[a]Abundance in inner ($T > 90$ K) region. 3σ upper confidence limit on the abundance in the outer envelope of 2×10^{-11}. [b]Upper limit to abundance in inner region ($T > 90$ K) assuming a low outer abundance of 1×10^{-15}. [c]As above but for inner region where $T > 30$ K.

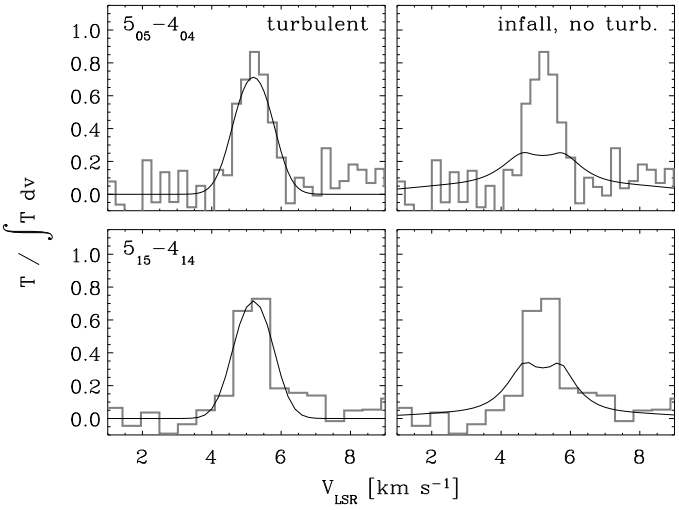

Figure 9.2. *Spectra and modeled line profiles of the $5_{05} - 4_{04}$ (para) and $5_{15} - 4_{14}$ (ortho) H_2CO lines (upper and lower panels, respectively) toward L1448-C in a pure turbulent, constant abundance envelope (this paper; left) and in a non-turbulent infalling envelope with an abundance jump (Maret et al. (2004a); right). The spectra have all been normalized by division with the total integrated line intensity to bring out more clearly the comparison between the actual line shapes.*

an increased abundance jump in the inner envelope up to 4 orders of magnitude. For both species a constant abundance model provides a good fit to the observed lines and the combination of the two suggests an ortho-para ratio of 1.6, in agreement with the conclusion above. In general, it is difficult to constrain the ortho-para ratio for a specific source because of the intrinsic uncertainty in the observations and modeling, including varying ortho-para ratios with position and varying optical depth (Schöier et al. 2002). The strength of the analysis presented in this paper is, however, that the ratio is based on a large sample of sources, statistically reducing some of these uncertainties.

The ortho-para ratio itself contains interesting information about the H_2CO formation, as discussed by Kahane et al. (1984). At high temperatures the ortho-para ratio approaches the relative statistical weights of 3:1, but thermalization at lower temperatures ($T \sim 10-15$ K) makes the two abundances closer to equal. As argued by Kahane et al., gas-phase thermalization is improbable: the life-times of the established ortho-para species are significantly longer than, e.g., destruction through reactions with molecular ions. Kahane et al. furthermore find that chemical reactions lead to ortho-para ratios of 3–5. In contrast, H_2CO can be thermalized on dust grains and released subsequently. For grain temperatures of 10–15 K, an ortho-para ratio of 1.5 is in good agreement with the results from this paper. This is also what is found in typical dark

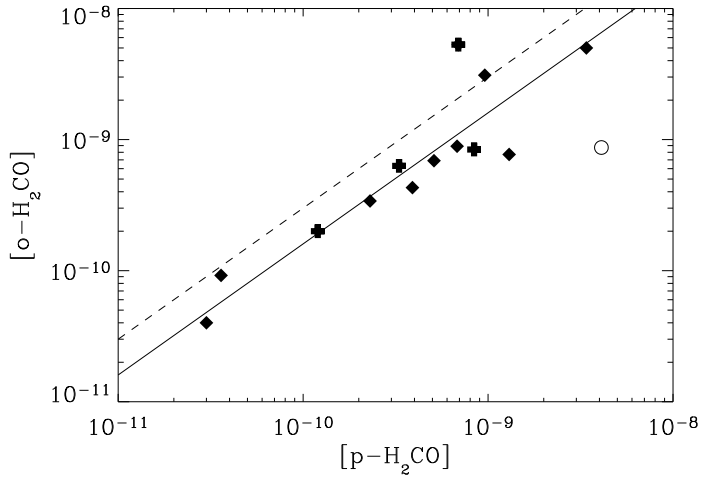

Figure 9.3. *Comparison between the abundances of the p-H_2CO and o-H_2CO species. Sources with poor fits ($\chi^2_{\rm red} \geq 5$) to either the p-H_2CO or o-H_2CO species are indicated by black crosses. Of these N1333-I4B has further been singled-out with the open circle. The solid line indicates the best fit linear correlation between the two sets of abundances (excluding the poorly fit sources), corresponding to an ortho-para ratio of 1.6:1. The dashed line indicates the relation for an ortho-para ratio of 3:1.*

clouds such as TMC1 and L134N, whereas warmer regions such as the Orion clouds show ortho-para ratios closer to the statistical 3:1 ratio (Kahane et al. 1984; Mangum & Wootten 1993).

Comparison to other molecules and implications for abundance structures

To quantify the relations between the abundances of the observed molecular species, Jørgensen et al. (2004d) calculated Pearson correlation coefficients for each pair of abundances. The Pearson correlation coefficient, P, is a measure of how well a (x, y) data set is fit by a linear correlation compared to the spread of (x, y) points. Values of ± 1 indicate good correlations (with positive or negative slopes) whereas a value of 0 indicates no correlation. In our studies of other molecules, strong correlations ($|P| \geq 0.7$) were found between molecules for which relations were expected based on chemical considerations, for example between CO and HCO^+ or between the sulfur-bearing species. To extend this discussion, correlation coefficients were calculated between the abundances found in this paper and those from Jørgensen et al. (2004d) (see Table 9.10).

An important conclusion is the apparent anti-correlation between the H_2CO abundances and envelope mass as shown in Fig. 9.5. This is also reflected in

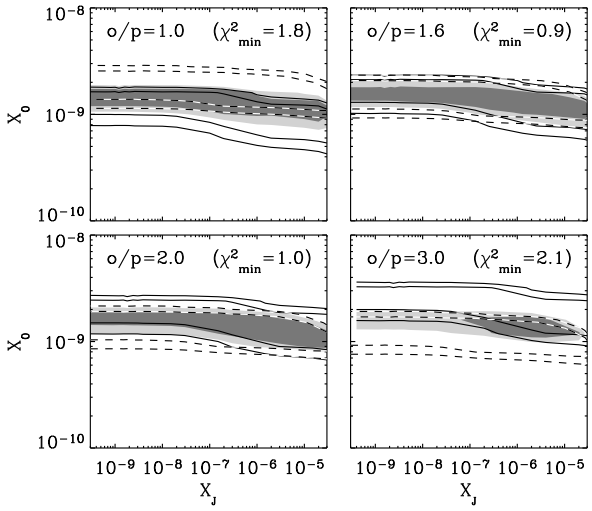

Figure 9.4. *Constraints on the H_2CO abundances in the inner ($T > 90$ K) and outer ($T < 90$ K) envelope (X_J and X_0, respectively) and effect of adopted ortho-para ratio for L1448-C. A non-turbulent, free-falling envelope has been adopted as in Maret et al. (2004a). The solid line contours indicate the 2 and 4σ confidence levels for ortho-H_2CO, whereas the dashed line contours indicate the corresponding confidence levels for p-H_2CO. The grey scale contours indicate similar confidence levels for the H_2CO abundance combining the constraints from the two datasets and assuming the ortho-para ratios of 1.0, 1.6, 2.0 and 3.0, respectively, as indicated in the top of each panel.*

Table 9.10. *Pearson correlation coefficients between abundances found in this paper and abundances from Jørgensen et al. (2004d).*

	p-H_2CO	o-H_2CO
CO	0.63	0.70
HCO^+	0.46	0.76
CS	0.42	0.60
SO	0.13	0.05
HCN	0.72	0.63
HNC	0.57	0.74
CN	0.57	0.81
HC_3N	0.44	0.70
p-H_2CO	...	0.92
o-H_2CO	0.92	...

the correlations in Table 9.10 between H_2CO and molecules such as CO whose abundances decline with increasing mass (Jørgensen et al. 2002). Jørgensen et al. (2004c,d) suggest a scenario in which the depletion occurs in a restricted part of the envelope, bounded outwards by the radius where the density becomes low ($n \leq n_{\rm de}$) so that the timescales become too long for freeze-out, and inwards by the radius where the temperature increases above the desorption temperature ($T \geq T_{\rm ev}$). The differences in H_2CO abundances for the observed sources then reflect the size of the region where freeze-out occurs.

As an illustration, the drop abundance scenario is tested for the H_2CO lines toward NGC 1333-IRAS4A. We first constrain the depletion density, $n_{\rm de}$, and desorption temperature, $T_{\rm ev}$, from observations of the CO lines presented by Jørgensen et al. (2002). The CO data toward NGC 1333-IRAS4A are well-fitted with depletion by a factor of 50 in the region of the envelope where the density is higher than 6×10^5 cm^{-3} and temperature lower than 40 K. These constraints are used as input for the H_2CO chemical structure, so that only the overall and depleted abundances, (X_0 and $X_{\rm D}$, respectively) are left as free parameters. The results of these fits are shown in Fig. 9.6: both ortho and para lines are consistent with an abundance drop of approximately an order of magnitude. The χ^2 confidence regions for the two H_2CO species agree at the 1σ level assuming an ortho-para ratio of 1.6. Also the o-$H_2^{13}CO$ observations agree with those of the main isotopic lines assuming a ^{12}C:^{13}C ratio of 70. The best fit drop model has an undepleted abundance $X_0 = 3 \times 10^{-9}$ and an abundance in the depletion region of $X_{\rm D} = 4 \times 10^{-10}$. The reduced χ^2 for this model is 1.1 for 10 fitted lines (including all ortho, para and $H_2^{13}CO$ lines). This suggests that the variations in H_2CO abundances reflect, to first order, the variations due to freeze-out, with the chemical network subsequently regulating the abundances. High-resolution interferometer observations confirm this structure for IRAS 16293-2422 and L1448-C (Schöier et al. 2004a).

Table 9.11 compares the drop abundance profiles for NGC 1333-IRAS4A with those of L1448-C and IRAS 16293-2422 (Schöier et al. 2004a). Similar values for X_0 are found within a factor 3 and with the H_2CO abundance decreased by an order of magnitude in the freeze-out zone. Also the maximum constant abundance for the entire sample is in agreement with this value for X_0, supporting the suggestion that the spread in constant H_2CO abundances reflects the size of the freeze-out zone.

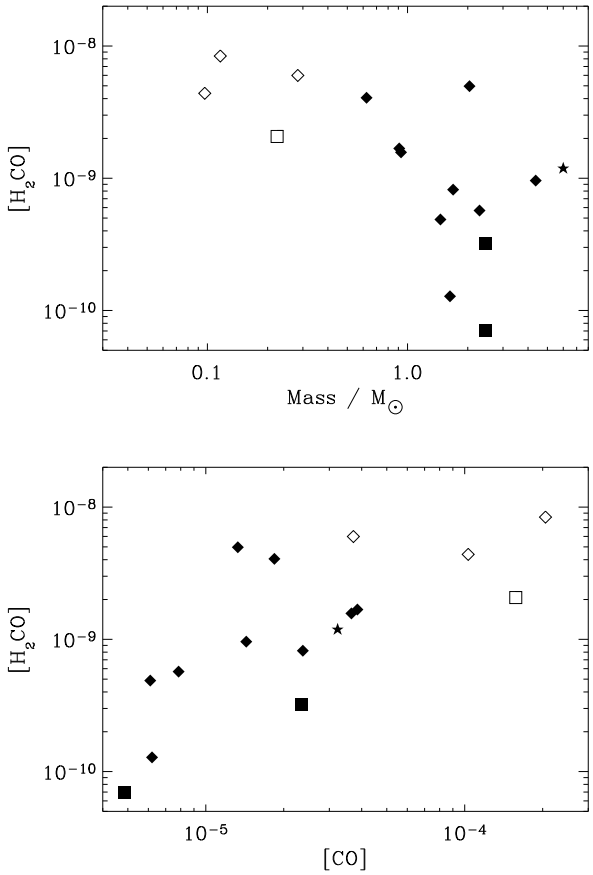

Figure 9.5. *Total H_2CO abundance vs. envelope mass (upper panel) and CO abundance (lower panel). For objects where only the abundance of one of the two H_2CO species has been constrained, an ortho-para ratio of 1.6 is assumed. the class 0 objects are indicated by "♦", the class I objects by "◊" and the pre-stellar cores by "■". The class 0 objects VLA1623 and IRAS 16293-2422 have been singled out by "□" and "★", respectively.*

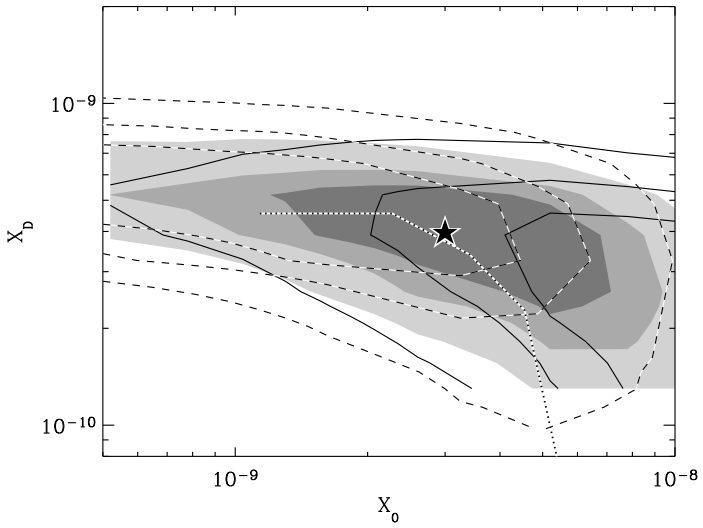

Figure 9.6. *Constraints on H_2CO abundances in a "drop" model for NGC 1333-IRAS4A, i.e., a model where the molecule is depleted to $X_{\rm D}$ in the regions where the density is higher than $n_{\rm de}$ and temperature lower than $T_{\rm ev}$ constrained from CO observations. The solid and dashed contours indicate the 1σ, 2σ and 4σ confidence levels for p-H_2CO and o-H_2CO, respectively whereas the grey-scale contours indicate the confidence region for the two species combined with an ortho-para ratio of 1.6. The black/white dotted line indicates the best fit relation from the o-$H_2^{13}CO$ lines. The best fit model (X_0=3×10^{-9}, $X_{\rm D}$=4×10^{-10}) combining all lines has $\chi^2_{\rm red}$ of 1.1 and is indicated with the "★".*

Table 9.11. *Summary of models with varying H_2CO abundance structure.*

	$X_{\rm D}$	X_0
NGC 1333-IRAS4A	4×10^{-10}	3×10^{-9}
L1448-C[a]	1×10^{-9}	1×10^{-8}
IRAS 16293-2422[a]	3×10^{-10}	1×10^{-8}
Sample[b]	7×10^{-11}	8×10^{-9}
NGC 1333-IRAS4B[c]	<1×10^{-9}	1×10^{-8}

[a]From Schöier et al. (2004a) fitting both single-dish and interferometer data. [b]Minimum and maximum abundances for the entire sample in this paper. [c]Model with abundance jump at 20 K. $X_{\rm D}$ for this source refer to the abundance where $T < 20$ K and X_0 to the abundance where $T > 20$ K.

A varying abundance structure is also preferred for NGC 1333-IRAS4B: as seen from Tables 9.5-9.6 and Fig. 9.3, the ortho-para ratio for this particular source is less than 1. This problem is not alleviated by the introduction of a "drop" profile, which still gives an ortho-para ratio below unity and a poor fit to, in particular, the ortho-H_2CO lines. An abundance increase at low temperatures, however, does a better job: Fig. 9.7 shows models for NGC 1333-IRAS4B with abundance jumps at differing temperatures. An abundance jump at $T_{\rm ev} \lesssim 30$ K from $\sim 10^{-10}$ to $\sim 10^{-8}$ makes it possible to fit the lines with an ortho-para ratio above unity, and to bring the abundance inferred from the o-$H_2^{13}CO$ lines in agreement with that of the o-$H_2^{12}CO$ lines. A jump at low temperatures also significantly improves the best fit for the two species separately. This is interesting compared with the results of Maret et al. (2004a) who inferred an abundance enhancement close to 4 orders of magnitude in NGC 1333-IRAS4B, but with a rather low quality of the fit ($\chi^2_{\rm red} \approx 7$). This suggests that the model with a jump at temperatures of 90-100 K is not adequate to describe the abundance structure for NGC 1333-IRAS4B but that other mechanisms such as the action of the protostellar outflow regulate the H_2CO abundance for this source.

To summarize these discussions: by fitting the ortho and para H_2CO lines independently for the larger sample of sources, the ortho-para ratio can be constrained statistically to be 1.6±0.3. The observed correlations with other species from the survey of Jørgensen et al. (2004d) suggest that the H_2CO abundances are related to the overall chemical network – primarily reflecting freeze-out of CO at low temperatures and high densities. This is further illustrated by fits to the NGC 1333-IRAS4A H_2CO data, which are improved with a "drop abundance" profile. In these models, the H_2CO abundance is decreased by an order of magnitude in the cold freeze-out zone. No jump in abundance in the innermost ($T \gtrsim 90$ K) region is needed, although NGC 1333-IRAS4B is best fit with an abundance increase where $T \gtrsim 20 - 30$ K. Observations of higher excitation lines are needed to constrain jumps in the hot core region. The NGC 1333-IRAS4B data suggest that for specific sources, other effects, such as the impact of the outflow, may play a role in defining the H_2CO abundance structures.

9.3.2 CH_3OH, CH_3CN and CH_3OCH_3

The upper limits for the constant CH_3OH abundances found for the sources in sample range from a few$\times 10^{-10}$ to $\sim 10^{-9}$. The upper limits are typically a factor of a few below the abundances determined from lower excitation CH_3OH lines by Buckle & Fuller (2002). However, since their abundances were calculated relative to CO, for which abundances are lower by an order of magnitude than the canonical value in the class 0 objects, the upper limits from this paper and the results of Buckle & Fuller (2002) are still consistent. Buckle & Fuller also found a slight decrease in CH_3OH abundance with bolometric temperature (i.e., lower CH_3OH abundance in the class I objects). This may again be a result of the abundance calculated relative to CO, since the CO abundance varies with envelope mass (Jørgensen et al. 2002). A similar trend was seen for

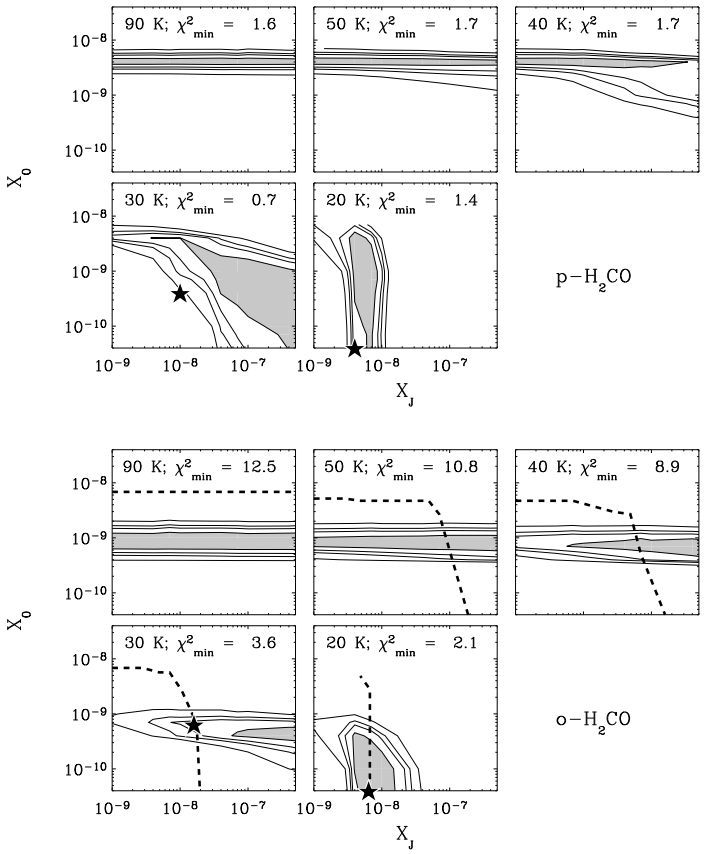

Figure 9.7. *χ^2-confidence contour plots for p-H_2CO and o-H_2CO abundances (upper and lower panels, respectively) toward NGC 1333-IRAS4B. The minimum $\chi^2_{\rm red}$ for the given jump temperature is indicated in the top of each panel. The dashed lines indicate the constraints on the abundances from the o-$H_2^{13}CO$ lines. In the $T_{\rm ev} = 20$ K and $T_{\rm ev} = 30$ K panels the best fit models combining the constraints for all lines (with minimum $\chi^2_{\rm red} = 1.7$ and 3.8, respectively) have been indicated by "★". For the other values of $T_{\rm ev}$, the minimum $\chi^2_{\rm red} > 5$.*

the sulfur-bearing species (Buckle & Fuller 2003, see discussion in Jørgensen et al. 2004d).

As noted by Maret et al. (2004b), the CH_3OH data for NGC 1333-IRAS2 and -IRAS4B (see also Tables 9.7-9.8) cannot be modeled with constant abundances. In the best cases such models give $\chi^2_{\rm red} \approx 10 - 20$. NGC 1333-IRAS4A also shows mediocre fits for each of the A and E-type species with constant abundances, but still better than the two other sources ($\chi^2_{\rm red} \approx 3 - 4$).

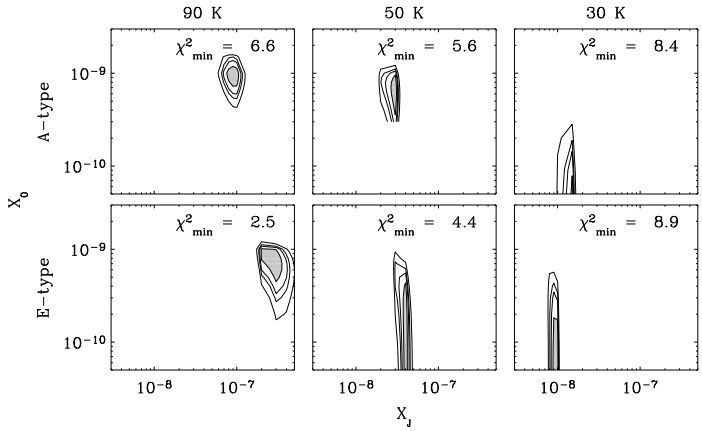

Figure 9.8. *χ^2-confidence contours for jump models with varying $T_{\rm ev}$ for CH_3OH lines toward NGC 1333-IRAS2. The minimum $\chi^2_{\rm red}$ is given in the upper right corner of each panel.*

Our analysis uses the new collisional rate coefficients for CH_3OH recently published by Pottage et al. (2004). Compared to the old rate coefficients, the derived line intensities vary in certain cases by up to 50%. However, no systematic trends are seen and therefore the derived abundance structures are unchanged. Still, this example illustrates that the derived abundances – especially when based on constraints from only a few lines – may be uncertain by up to a factor of 2 due to uncertainties in the collisional data alone (see also Schöier et al. 2004b).

The poor fits can be improved by including evaporation of grain ice mantles at temperatures $\gtrsim 90$ K (Ceccarelli et al. 2000a; Schöier et al. 2002; Maret et al. 2004a,b). To test this, a step function for the abundance was introduced, with a jump in abundance from X_0 in the exterior to $X_{\rm J}$ in the interior at a radius corresponding to a specific temperature $T_{\rm ev}$. Models were run for $T_{\rm ev} = 30$, 50 and 90 K for each of the three NGC 1333 sources. Table 9.12 gives the best fit models and Fig. 9.8-9.10 show the derived χ^2 confidence plots for each of the temperatures and for each of the sources. They clearly show different behavior: NGC 1333-IRAS2 is nicely fit with a jump at 90 K, whereas NGC 1333-IRAS4B is much better fit with a jump at 30 K. For NGC 1333-IRAS4A the models suggest a best fit for a constant or anti-jump abundance structure (i.e., a decrease in abundance in the innermost regions).

It is also noteworthy that the best fits of both A- and E-type species are obtained for similar abundances at the best fitting evaporation temperatures. As for the H_2CO ortho-para species, no transitions between the A- and E-type CH_3OH levels are expected. The E/A-type abundance ratio, however, only varies from 0.69, corresponding to thermalization at 10 K, to unity in the high

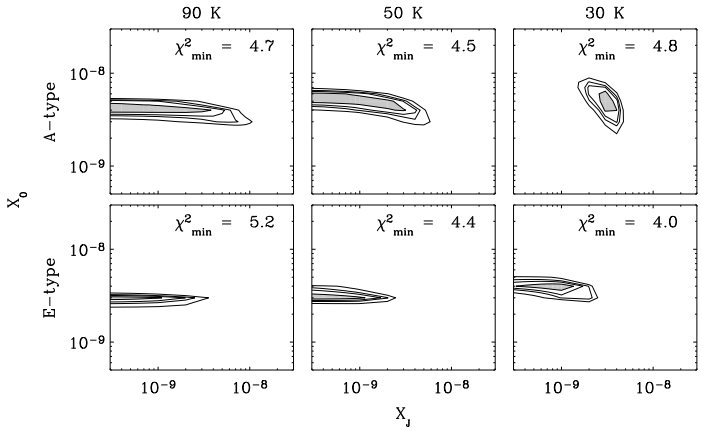

Figure 9.9. *As in Fig. 9.8 for CH_3OH lines toward NGC 1333-IRAS4A.*

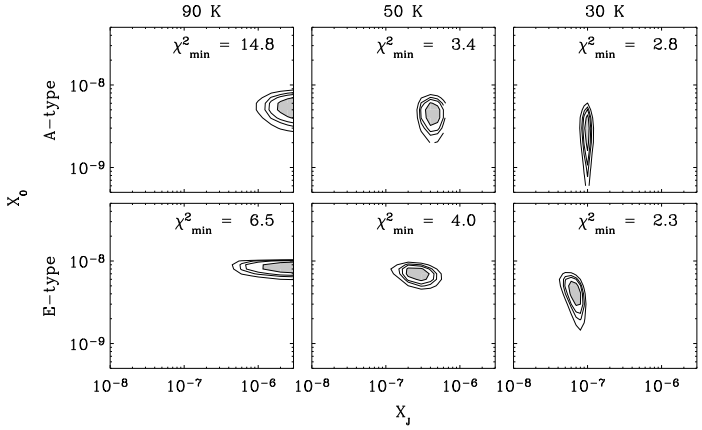

Figure 9.10. *As in Fig. 9.8 for CH_3OH lines toward NGC 1333-IRAS4B.*

temperature limit (Friberg et al. 1988). The abundances are therefore expected to be similar for the best fit models, which appears to be the case as illustrated in Fig. 9.8-9.10.

For NGC 1333-IRAS2 similar jump models were run for CH_3CN, and the best fit abundance is shown in Fig. 9.11. Interestingly the CH_3CN lines also give an abundance jump of approximately two orders of magnitude at 90 K, similar to what is found for the CH_3OH lines. Again jumps at lower temperatures are not favored for this source.

The upper limits for CH_3OCH_3 and CH_3CN were also used to derive up-

Table 9.12. *Derived CH_3OH and CH_3CN abundances assuming abundance jumps in the inner $T > T_{\rm ev}$ regions.*

	$T_{\rm ev}$	Species	$X_{\rm J}$	X_0	$\chi^2_{\rm red}$
		CH_3OH			
IRAS2	90 K	A-type (8)	9×10^{-8}	1×10^{-9}	6.6
		E-type (13)	3×10^{-7}	7×10^{-10}	2.5
IRAS4A	50 K	A-type (7)	$\leq5\times10^{-9}$	4×10^{-9}	4.5[a]
		E-type (7)	$\leq2\times10^{-9}$	3×10^{-9}	4.4[a]
IRAS4B	30 K	A-type (7)	1×10^{-7}	3×10^{-9}	2.8
		E-type (7)	9×10^{-8}	3×10^{-9}	2.7
IRAS 16293-2422[b]	90 K	A+E-type (23)	1×10^{-7}	6×10^{-9}	1.2
		CH_3CN			
IRAS2	90 K	A-type	7×10^{-9}	$< 3\times10^{-11}$	1.4

[a]No strong constraints exist on the evaporation temperature for NGC 1333-IRAS4A in accordance with the conclusion that this source is well-fitted by a constant abundance throughout the envelope (see Fig. 9.9). [b]Results for IRAS 16293-2422 from Schöier et al. (2002) assuming the abundances of the A- and E-type CH_3OH to be identical.

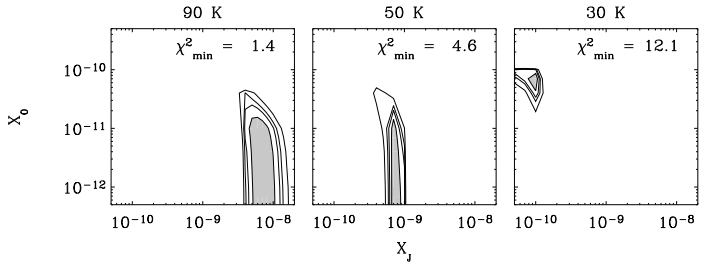

Figure 9.11. *χ^2-confidence contours for jump models with varying $T_{\rm ev}$ for CH_3CN lines toward NGC 1333-IRAS2. The minimum $\chi^2_{\rm red}$ is given in the upper right corner of each panel.*

per limits on the abundances in the innermost regions for the sources where the lines are not detected. The integrated intensity limits for the NGC 1333 sources are a factor of 10 lower than those for IRAS 16293-2422 for similar lines observed with the JCMT, but the abundances are less affected due to the larger distance (220 pc vs. 160 pc) and lower luminosity (16 vs. 27 $L_\odot$). The re-

sults for models with constant abundances (first entry) and abundance jumps at 90 K (second entry) are given in Table 9.9. For the "jump models" complete depletion was assumed at temperatures below 90 K. These constant abundance and jump models therefore represent the two extremes. For CH_3CN, the value of $X_{\rm J}$ for NGC 1333-IRAS2 is comparable to that derived for IRAS 16293-2422 by Schöier et al. (2002) and Cazaux et al. (2003). NGC 1333-IRAS4A may have CH_3CN abundances that are a factor of 10 lower. For CH_3OCH_3 the upper limits to the line intensities restricts a constant abundance to $\lesssim$a few $\times 10^{-9}$ for the three NGC 1333 sources. Meaningful limits on the CH_3OCH_3 abundance in the innermost region cannot be derived from these observations, however, due to the line becoming optically thick. No strong evidence therefore suggest that the chemistry of these species is significantly different in the innermost envelopes around the objects discussed in this paper compared to IRAS 16293-2422.

9.4 Discussion

9.4.1 Hot core vs. outflow

As discussed in Sect. 9.3.1, the H_2CO abundances are found to be consistent with constant abundances throughout the envelopes for most sources. The CH_3OH results for the three NGC 1333 sources, in contrast, imply abundance variations, but these occur over significantly different regions of the envelope. The three objects have rather similar density and temperature profiles and the observed differences therefore suggest other causes for the abundance enhancements than passive heating of the envelope material.

An important clue comes from the H_2CO and CH_3OH line profiles. Fig. 9.12 compares the profiles for the H_2CO $5_{05} - 4_{04}$ and CH_3OH $7_{-1} - 6_{-1}$-E lines toward NGC 1333-IRAS2. The CH_3OH line is significantly broader, with a width of 4 km s^{-1} compared to the 1.5 km s^{-1} for the H_2CO line. Part of this could be due to differences in the thermal broadening if CH_3OH probes warmer gas much deeper in the envelope. The radiative transfer models, however, take this explicitly into account and it is concluded that a significantly higher turbulent broadening is required to model the observed CH_3OH lines compared with those of H_2CO and other species. This suggests that the CH_3OH lines probe a different part of the envelope than H_2CO and the species discussed by Jørgensen et al. (2004d).

One explanation for the enhancements and profiles of CH_3OH could be the impact of the outflows on the inner envelopes. This was suggested to be the case for NGC 1333-IRAS4A and IRAS4B by Blake et al. (1995), who noted that the abundance enhancements can occur in the outflow shear zones probed by the very broad, kinematically distinct CS and CH_3OH lines. Large enhancements of CH_3OH are seen in the shocks driven by the outflows from protostellar sources such as L1448-C, L1157 and NGC 1333-IRAS2 (Bachiller et al. 1995; Bachiller & Pérez Gutiérrez 1997; Jørgensen et al. 2004a) where the shock is well separated from the central protostar. CH_3OH is one of the molecules

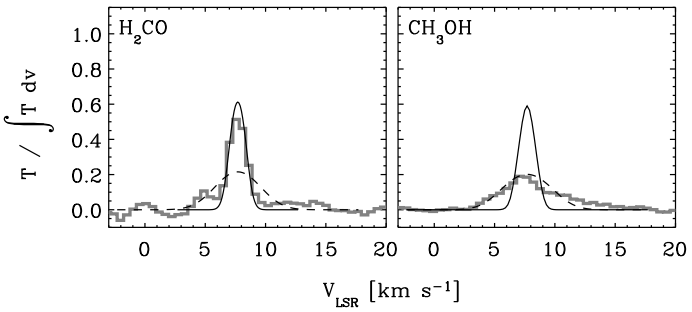

Figure 9.12. *Observed and modeled spectra of the H_2CO $5_{05} - 4_{04}$ and CH_3OH $7_{-1} - 6_{-1}$-E lines toward NGC 1333-IRAS2. The two models shown use turbulent line broadening of 0.8 km s^{-1}, which can also account for, e.g., the $C^{18}O$ lines modeled in Jørgensen et al. (2002) (solid line) and 2.5 km s^{-1}(dashed line), respectively. Note how the two lines probe significantly different velocity fields in the envelope.*

that shows the largest jumps in abundances between cold and warm gas and therefore traces more clearly the origin of the abundance enhancements.

An outflow scenario could explain the relatively low desorption temperature found for the CH_3OH lines as well as the fits to the H_2CO lines for NGC 1333-IRAS4B discussed in Sect. 9.3.1. If these species are desorbed from grains due to the action of the outflow, they could thermalize at temperatures closer to that of the envelope, i.e., lower than in the small "hot core" region. NGC 1333-IRAS4A is remarkable since the fits to the CH_3OH lines do not require a jump in abundance. This difference from NGC 1333-IRAS4B could be caused by the differences in the outflow morphologies: Di Francesco et al. (2001) imaged the NGC 1333-IRAS4 region at high resolution and found that the outflows are probed by the wings of H_2CO and CS. The images show that the IRAS4B outflow is more compact, with emission over a $\approx 15''$ region comparable to the 350 GHz JCMT single-dish beam. The morphology thus suggests that enhancements for the NGC 1333-IRAS4B outflow occur on scales where the single-dish observations are the most sensitive. Also the SiO J =5–4 line at 217.1 GHz is only detected toward NGC 1333-IRAS4A and not IRAS4B. This indicates that the CH_3OH enhancements in IRAS4B are not directly associated with a high velocity shock but more likely result from the shear between the envelope and outflow. Note also that direct images of outflow induced shocks (Bachiller & Pérez Gutiérrez 1997; Garay et al. 2000; Bachiller et al. 2001; Jørgensen et al. 2004a) indicate that CH_3OH does not survive at the highest shock speeds, which could further explain the differences between IRAS4A and IRAS4B.

9.4.2 Comparison with IRAS 16293-2422

The above results again raise the question what causes the richness of lines in IRAS 16293-2422, since its abundances in the outer envelope are comparable to those of other sources. One explanation may be that its small-scale physical structure is significantly different from that of the remaining sources. The central binary system has a separation of 8-10″ and affects the material in the envelope with emission from the various species centered around one or both components (Mundy et al. 1992; Schöier et al. 2004a). Furthermore the circumbinary envelope appears to have an inner cavity of size comparable to the binary separation. It may be that this relatively wide (∼1000 AU) binary pushes material to larger distances where it can more easily be observed through single-dish observations with ∼10–15″ beams. Alternatively, the circumbinary envelope may be heated on larger scales through each of the relatively luminous components compared with that expected from a single component in a simple spherical envelope. Finally, interferometer maps also show velocity gradients indicating that the outflow affects the envelope material close to the central protostar. It is possible that the outflow processing leads to abundance enhancements of the organic species on larger scales than the passively heated hot core, thus providing a larger filling factor of the single-dish beam.

9.4.3 High excitation CS and HDO lines as dense gas probes

Further support for this interpretation comes from observations of high excitation CS $J = 10 - 9$ and HDO lines obtained with the JCMT. For CS $J = 10 - 9$, broad lines (FWHM ≈ 8 km s^{-1}) are detected toward both NGC 1333-IRAS4A and IRAS4B, which lack the central narrow peak seen for the lower excitation lines (see Fig. 9.13). Although, the absolute calibration may be somewhat uncertain, the CS $J = 10 - 9$ line is approximately 5 times stronger toward IRAS4B than IRAS4A. This is in contrast to the lower excitation CS lines reported, e.g., by Blake et al. (1995) and Jørgensen et al. (2004d), which supports a more compact origin of the CS outflow emission in IRAS4B than IRAS4A. Table 9.13 compares the predictions for the CS $J = 10 - 9$ line intensity assuming CS abundances in the quiescent envelope from the models of Jørgensen et al. (2004d). The envelope models predict significantly less emission than observed for IRAS4A and IRAS4B, but the non-detection toward IRAS2 is consistent within the 3σ noise level. Note that the CS intensities in Jørgensen et al. (2004d) were found by integration over ± 2 km s^{-1} from the systemic velocity: for the CS $J = 10 - 9$ lines the emission integrated over this velocity range only contributes 20–25% of the total integrated emission and is still underestimated by the envelope models, especially for IRAS4B. Again this suggests that the observed CS $J = 10 - 9$ emission probes different material than traced in the bulk envelope material.

Another simple estimate can be made assuming that the CS emission comes

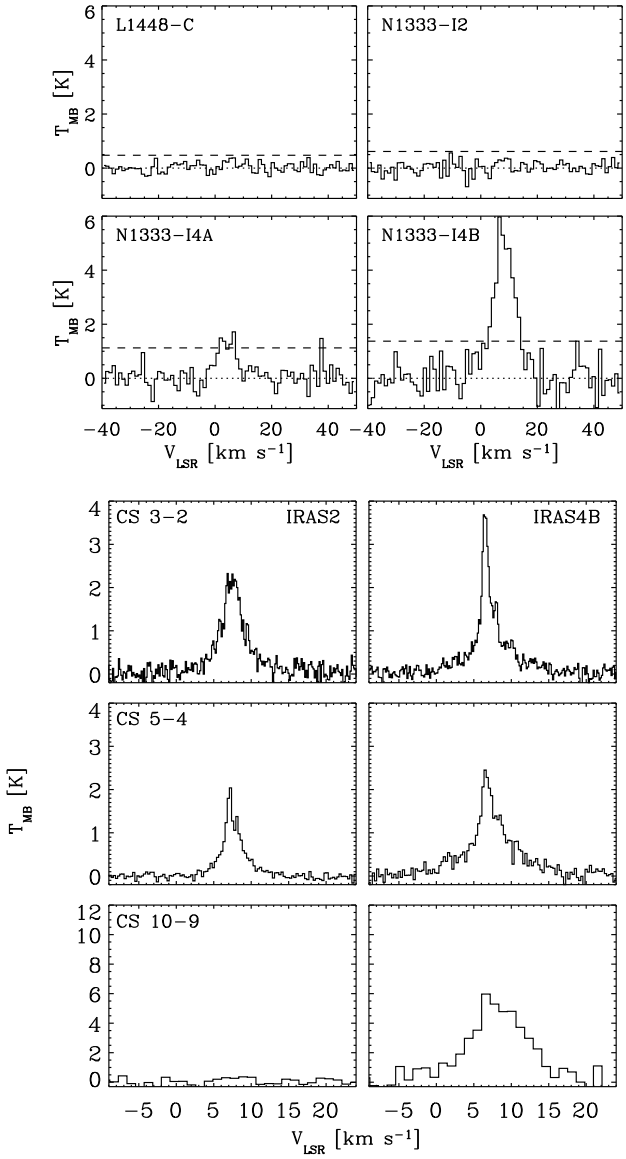

Figure 9.13. *Upper 4 panels: CS $J = 10 - 9$ observations of L1448-C and the three NGC 1333 sources. In each plot the dashed line indicates the 3σ detection limit. Lower 6 panels: Comparison between CS lines probing different excitation conditions in the envelopes, i.e., depths of NGC 1333-IRAS2 and -IRAS4B. The lowest excitation 3–2 lines are from IRAM 30 m observations the remainder from JCMT observations.*

Table 9.13. *Observed and predicted line intensities* ($\int T_{\rm MB}\,{\rm d}v$) *for CS* $J = 10-9$ *for the three sources in NGC 1333.*

Source	$I_{\rm mod}$ [K km s^{-1}]^a	$I_{\rm obs}$ [K km s^{-1}]^b
IRAS2	1.8	< 2
IRAS4A	1.7	12 (3)
IRAS4B	1.1	51 (11)

^{a}Predicted CS $J = 10 - 9$ line intensity adopting best fit abundances for each source from Jørgensen et al. (2004d). ^{b}Total line emission from Gaussian fits (IRAS4A and IRAS4B) or as 3σ upper limit (IRAS2). For IRAS4A and IRAS4B the number in parenthesis indicate the line emission integrated over ± 2 km s^{-1} from the systemic velocity.

from a medium with a constant density and kinetic temperature. Using a non-LTE escape probability code, *Radex* (Jansen et al. 1994; Schöier et al. 2004b), the CS column density is estimated adopting a density of 3×10^6 cm^{-3} and kinetic temperature of 100 K (Blake et al. 1995), consistent with the intensity of the wing emission from the CS 5–4 and 7–6 lines from Jørgensen et al. (2004d). A high column density of $\sim 5 \times 10^{14}$ cm^{-2} is needed to produce the observed CS 10–9 emission. Even at such high column densities, the emission is found to be optically thin. This column density is an order of magnitude larger than found from the lower excitation lines by Blake et al. (1995) and corresponds to $\approx 5 - 10\%$ of the estimated CO abundance in the outflowing material.

In contrast to the CS $J = 10 - 9$ lines, HDO $2_{11} - 2_{12}$ is detected only toward NGC 1333-IRAS2 and not IRAS4A and IRAS4B (see Fig. 9.14). This line probes the warm gas with an upper level energy of 90 K. The observed line is narrow (FWHM of ≈ 2.5 km s^{-1}) compared to the ≈ 8 km s^{-1} for the CS $J = 10 - 9$ and ≈ 4 km s^{-1} for the CH_3OH lines toward IRAS4A and IRAS4B. This suggests that this line has its origin in a "hot inner region" of the NGC 1333-IRAS2 envelope, although relation to the small-scale outflow (as seen in high resolution maps by Jørgensen et al. 2004b) cannot be ruled out. Enhancements of HDO by up to a factor of 10 were derived for the IRAS 16293-2422 outflow by Stark et al. (2004). Observations of more transitions will be needed before either scenario can be confirmed or ruled out. Since both CH_3OH and CH_3CN observations indicate the presence of warm gas with abundance jumps in the inner ($T < 90$ K) region, NGC 1333-IRAS2 still seems the best candidate for further comparative studies of the passively heated, hot inner regions of low-mass protostellar envelopes.

9.5 Conclusions

We have presented an analysis of H_2CO and CH_3OH line observations for a sample of 18 pre- and protostellar cores which have previously been studied

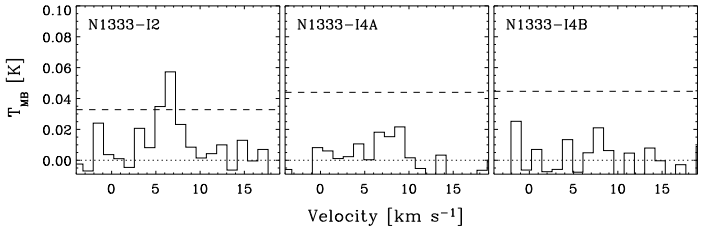

Figure 9.14. *Observations of the HDO $2_{11} - 2_{12}$ line at 241.5616 GHz toward the three NGC 1333 sources observed in the CH_3OH $5 - 4$ setting. HDO is only detected toward NGC 1333-IRAS2. In each plot the dashed line indicates the 3σ detection limit.*

through continuum and line observations and detailed radiative transfer modeling (Jørgensen et al. 2002, 2004d). These results complement the results by Maret et al. (2004a,b) for a subset of sources. In addition, observations and limits for high excitation CS $J = 10 - 9$ transitions and lines of HDO, CH_3CN and CH_3OCH_3 are presented for a subset of sources. Molecular abundances are derived through Monte Carlo line radiative transfer and compared to the results from the survey of Jørgensen et al. (2004d). The main conclusions are:

- The H_2CO data of most sources can be well-fitted by constant abundances throughout their envelopes if the ortho-para ratio is lowered to 1.6$\pm$0.3. This implies thermalization of H_2CO at low temperatures, e.g., on grain ice-mantles. Higher angular resolution data are needed to constrain the presence of any abundance jumps in the inner warm envelopes.

- The H_2CO abundances are related to the chemical network of the other species indicating that the same processes regulate their abundances. As an example the H_2CO data for NGC 1333-IRAS4A are well-fit by "drop abundance" profiles with a decrease in abundance in a limited part of the envelope, bounded inwards by the desorption temperature and outwards by a density corresponding to the timescale of the core. A counter example is provided by NGC 1333-IRAS4B, where an abundance increase is only needed where the temperature rises above 20–30 K with no enhancement in the outermost regions. This indicates that for some sources other effects, such as the impact of an outflow, may be important for regulating the H_2CO abundances.

- The upper limits to the CH_3OH abundances for the entire sample are a few$\times 10^{-10}$–10^{-9}. These results are consistent with actual abundances determined by Buckle & Fuller (2002) from lower excitation lines.

- CH_3OH observations for NGC 1333-IRAS2 and NGC 1333-IRAS4B require abundance jumps at 90 K and 30 K, respectively. Together with the significantly broader lines of CH_3OH compared with H_2CO and other

species, this suggests that the abundance increase for NGC 1333-IRAS4B, in particular, is due to a compact outflow interacting with the nearby envelope. This is further supported by the broad high frequency CS $J = 10 - 9$ line, detected very strongly toward this source. HDO and CH_3CN, in contrast, are only observed for NGC 1333-IRAS2 - possibly reflecting the presence of a passively heated, warm inner region for this source where molecules can evaporate. The CH_3CN data for NGC 1333-IRAS2 also require a jump in abundance at 90 K by about two orders of magnitude.

- For NGC 1333-IRAS4A, upper limits for the CH_3CN abundance in the warm inner region are somewhat lower than the abundances in NGC 1333-IRAS2 and IRAS 16293-2422. Still, no evidence suggests that the chemistry of this molecule, and CH_3OCH_3, in the envelopes around the objects discussed in this paper differs significantly from that in IRAS 16293-2422.

This chapter reinforces the importance of identifying (if possible) unique chemical tracers of material heated "passively" by a central protostar and by shocked material in outflows. Even relatively high excitation lines from single-dish observations (such as the CS $J = 10 - 9$ lines) may be affected by the outflow and can provide a good indication of the filling factor of dense shocked material. Future Herschel-HIFI observations may provide additional tests of the chemical structure by observations of high frequency lines, but the overlap between the shock and envelope chemistry may be problematic for these large beam data. Possibly the best way of distinguishing the different chemical scenarios will be through high angular resolution, high excitation observations with facilities such as the SMA and ALMA - or from studies of outflows well-separated from the central protostar as, for example, done in Bachiller & Pérez Gutiérrez (1997) and Jørgensen et al. (2004a). Better knowledge about the physical properties of the inner envelopes will also be important, since the adopted envelope models are extrapolations from the larger-scale observations of the cold dust in the outer envelope. Infrared observations with the Spitzer Space Telescope can place better constraints there.

Acknowledgements

The authors thank Sebastien Maret and Cecilia Ceccarelli for interesting discussions and communicating their results prior to publication. The research of JKJ is funded by a NOVA network 2 Ph.D. stipend. FLS acknowledges support from the Swedish Research Council. Astrochemistry research in Leiden is supported by an NWO Spinoza grant.